Heat and Mass Transfer (2024) 60:147–165
https://doi.org/10.1007/s00231-023-03416-1

ORIGINAL ARTICLE

Numerical study of the effects of bifurcation angle on hemodynamics during pulsatile flow in a carotid artery bifurcation

Damini Singh[1] · Sarita Singh[1]

Received: 17 March 2023 / Accepted: 2 August 2023 / Published online: 19 September 2023

Abstract

To investigate the effects of the hemodynamics of arterial shape, mainly the bifurcation angle and sinus shape of the carotid artery, a computational model of the carotid artery has been constructed. In this research, we evaluate the distribution of velocity, pressure, and wall shear stress (WSS), time average wall shear stress (TAWSS) and oscillatory shear index (OSI). Three different carotid artery models with varying bifurcation angles with 33° with normal sinus shape, 45° with elliptical sinus shape and 63.3° with cylindrical sinus shapes have been subjected to computational fluid dynamics simulations. The research focuses on flow and stress characteristics in the carotid sinus. This study employs the fundamental equation of fluid mechanics, known as the Navier-Stokes equations, as the governing equation to assess hemodynamic parameters and determine blood flow characteristics. The simulation used the pressure correction finite volume method. For the non-Newtonian behaviour of blood, the Carreau model is used based on the measured dynamic viscosity. For pulsatile flow, a representative standard carotid artery bifurcation pulse wave is applied at the inlet of the common carotid artery model. The results show that the wider angle model exhibits a low WSS while the narrow angle model demonstrates a high WSS, indicating a high-risk area for atherosclerosis plaque, and regions with low and oscillatory shear stress in the carotid artery can lead to endothelial dysfunction.

Abbreviation

BA	Bifurcation Angle
CCA	Common Carotid Artery
CFD	Computational Fluid Dynamics
ECA	External Carotid Artery
ICA	Internal Carotid Artery
SIMPLEC	Semi Implicit Method for Pressure-Linked Equations Consistent
SIMPLE	Semi-Implicit Method for Pressure Linked Equations
UDF	User Define Method
WSS	Wall Shear Stress
TAWSS	Time Average Wall Shear Stress
OSI	Oscillatory Shear Indez

Nomenclature

σ	Component of Stress Tensor
μ	Dynamic Viscodity
ρ	Fluid Density
n	Power Index
λ	Relaxation Time
$\dot{\gamma}$	Shear Rate
μ_∞	Viscosity at zero shear rate (Pa.s)
μ_0	Viscosity at Zero Shear Rate (Pa.s)
τ	Yield stress
$k-\epsilon$	Standard $k-\epsilon$ Model

1 Introduction

Understanding the role of hemodynamics in the onset of atherosclerosis and the treatment of vascular diseases is of utmost importance. Stroke, a prevalent arterial condition, stands as a leading cause of mortality worldwide [1]. Within the carotid artery, two primary branches, namely the internal carotid artery (ICA) and the external carotid artery (ECA), stem from the common carotid artery (CCA). Positioned upstream of the bifurcation, the CCA serves as the entry point, allowing blood to enter the system [2–4]. Conversely, the ICA and ECA, situated downstream of the bifurcation,

✉ Sarita Singh
saritamath@gmail.com

Damini Singh
damini.ds84@gmail.com

[1] Department of Mathematics, School of Physical Sciences, Doon University, Dehradun, Uttarakhand 248001, India

function as the exit arteries, through which blood leaves the body. Notably, the internal carotid artery encompasses a slightly expanded segment called the carotid sinus, positioned shortly after the bifurcation. The carotid sinus operates as a pressure receptor and regulator [5–7]. From a fluid-dynamic perspective, the flow in this region experiences significant disturbances. Existing literature suggests that flow separation and recirculation play vital roles in the formation of platelet thrombus and the early development of atherosclerotic plaques [8].

The utilization of computational fluid dynamics (CFD) has proven instrumental in the investigation of hemodynamics at the common carotid bifurcation, enabling an enhanced analytical exploration of the intricate interplay between vascular disease and hemodynamics. Due to its ability to offer thorough insights into blood flow characteristics and related phenomena, this innovative approach has grown significantly popularity in hemodynamic research. Using computational fluid dynamics (CFD), researchers can model and analyse the intricate fluid dynamics that occur around the carotid artery bifurcation, exposing the underlying causes of cardiovascular diseases. A comprehensive framework for examining hemodynamic variables, flow patterns, and distributions of wall shear stress that are closely associated with the initiation and development of vascular diseases is provided by the use of CFD in hemodynamic investigations [9, 10].

The carotid artery is a convoluted vessel with multiple twists, branching, and sections of varied diameters, rather than a simple straight tube. The geometry of the artery influences how blood flows through it. The shear stress exerted on the arterial wall by blood flow is one of the primary mechanical variables involved. Shear stress is the force that acts parallel to the wall of the vessel. When blood flows through the curved and irregularly shaped carotid artery, it experiences variations in flow velocity and pressure. These variations in flow dynamics lead to fluctuations in shear stress along the arterial wall. Numerous studies have suggested a close correlation between atherosclerosis invocation and bifurcation geometry with unique structures, such as the division of the common carotid artery (CCA) into daughter arteries of varying size, structure, and branching angle (the angle between the internal carotid artery (ICA) and external carotid artery (ECA)) [11]. In clinical contexts, the bifurcation angle (BA), which is the angle between the daughter vessels after branching, has been proposed as a risk predictor. [12–15]. Tada [16] studied the effect of changing the bifurcation angle on the distribution and level of both WSS at the encountered site of atherosclerotic lesions in the carotid bifurcation. Their findings revealed that variations in the bifurcation angle had a substantial impact on the distribution of both WSS and the dimensionless oxygen wall flux. However, it was discovered that changing the bifurcation angle had only a modest impact on the axial flow pattern. Ro and Ryou [17] conducted a numerical analysis that focuses on the characteristics of blood flow in a stenotic artery bifurcation when subjected to human body acceleration. The analysis included six simulation cases with varying body accelerations and bifurcation angles. The objective was to determine how these variables affected flow rate and wall shear stress. According to the results of research, increasing body acceleration caused an increase in both flow rate and wall shear stress. Using computed CT angiograms, Sun and Cao, [13], investigated the relationship between angle and plaque development in 22 individuals with left main disease. They found a connection between a significant bifurcation angle and changes in dimension downstream of the lesion. Momin et al. [18] used three different left carotid artery geometries with angles of 40°, 48.5°, and 63.5° to study the influence of hematocrit (Hct) level and bifurcation angle on the onset of atherosclerosis. The study also found that models with wider angles had lower WSS values and models with narrower angles had higher WSS values. Using computational methods, Zalud et al. [19] studied the impact of vessel form on the distribution of wall shear stress. This was achieved by contrasting flow patterns and wall shear stress measurements between a high-risk predisposition anatomy and a low-risk carotid artery bifurcation geometry. The aim of this research was to investigate the precise effects of vascular geometry on the distribution of wall shear stress, as well as any potential implications for the establishment of high-risk conditions at the carotid artery bifurcation. According to their findings, the internal carotid artery's branching angle is greater in high-risk individuals, and there is a reduced relationship between the diameter of the internal carotid artery and the diameter of the carotid artery. The fluid flow and stress in the carotid artery have been the subject of extensive experimental and theoretical investigation. The carotid sinus flow happens, according to the flow dynamics studies [16, 20, 21]. The flow characteristics of the sinus throughout the pulse cycle are sensitive to the bifurcation angle in this study. It was attempted, in particular, to assess the role of the bifurcation angle in atherogenesis by correlating variations in bifurcation geometry with changes in low pattern, WSS distributions [22].

Understanding the impact of variable bifurcation angle and sinus shape on atherosclerosis formation is crucial for gaining comprehensive insights into the development and progression of this cardiovascular disease. However, there is still limited knowledge regarding the specific influence of variable bifurcation angle and sinus shape on atherosclerosis formation in bifurcation geometries. To the best of our knowledge, no study has been conducted to investigate this correlation. Hence, in the present study, an attempt made on elucidating the effects of variable bifurcation angle and sinus shape simultaneously on atherosclerosis formation in bifurcation geometries would be a valuable addition to the existing knowledge. Three idealised geometries of the

carotid bifurcation model with a standard "Y" bifurcation shape are selected, with variation in only the bifurcation angle and sinus shape to minimise the other shape-induced flow effects. Indeed, analyzing the influence of variable bifurcation angle and sinus shape on local hemodynamics, including parameters such as velocity profile, wall shear stress (WSS), time-averaged wall shear stress (TAWSS), oscillatory shear index (OSI), can provide valuable insights into the clinical implications and potential outcomes. The findings reveal that the model with a wider angle experiences reduced wall shear stress (WSS), while the model with a narrower angle experiences elevated WSS, signifying a high-risk region for atherosclerosis plaque formation. Additionally, low and oscillatory shear stress in the carotid artery's certain areas can trigger endothelial dysfunction, which refers to impairment of the inner arterial lining.

The structure of this work is as follows: Section 2 is the methodology section, which describes the approach we used to carry out the study. This section consists of the geometrical model used in the study, along with the governing equations, non-Newtonian viscosity model, boundary conditions, and numerical method used to simulate the system under investigation. Simulation results and a discussion of the implications of their findings are presented in Section 3. Finally, Section 4 provides a summary of the conclusions.

2 Methodology

2.1 Geometrical model and flow conditions

In this study, Three carotid artery models were developed for the study, each representing different geometries. 3D models is used to simulate numerical flow in the bifurcation of the carotid artery. The geometry of the three bifurcation models is shown in Fig. 1. where the 3D representation is displayed with different in the bifurcated angle, Model 1, Model 2 and Model 3. The Model 1 and Model 2 are the CAD models constructed in ANSYS Design Modular, and Model 3 is the realistic geometry of the carotid artery [23].

1. Model 1: Bifurcation angle 45°, Sinus Shape: Elliptical
2. Model 2: Bifurcation angle 63.3°, Sinus Shape: Cylindrical
3. Model 3: Bifurcation angle 33°, Sinus Shape: Normal

The geometric parameters of the carotid artery model were derived from [24]. The essential geometrical parameters are diameter of CCA, i.e. $D = 8$ mm and ECA diameter $0.5775D$ and the diameter of ICA is $0.69375D$ and the length of the CCA is $5.125D$, and the lengths of ECA and ICA are the

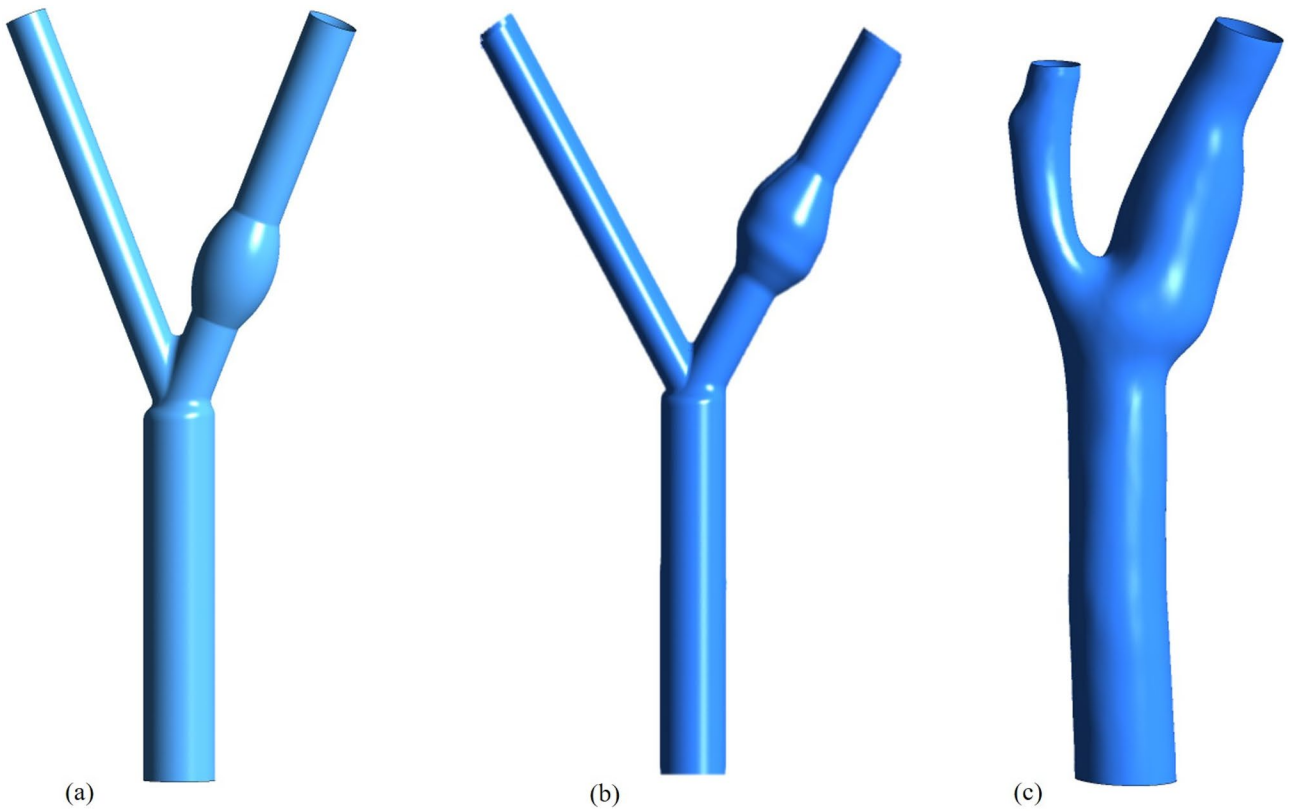

Fig. 1 Models

same i.e 5.875D. Carotid artery geometrical model 1 and model 2 have the angle between the external carotid artery and the internal carotid artery. The sinus region in the internal carotid artery is constructed using an ellipsoid, which has a major axis of 18.27 mm and a minor axis of 8 mm [25] and the centre of the ellipsoid is located at 15 mm away from the bifurcation point.

We have considered 6 different cross-section locations where numerical results are presented, as shown in Fig. 2. Line 1 is at a distance of 21 mm from the inlet, which is the midpoint of the CCA, line 2 is at 42 mm, at the bifurcation of the artery. Lines 3, 4, 5, and 6 are located in the sinus region; the spacing between these lines is 5 mm.

2.2 Mathematical modeling and computational setup

2.2.1 Governing equations

In this study, the mathematical simulation is based upon three-dimensional non-linear Navier-Stokes equations for incompressible, non-Newtonian flow fields that are time-dependent [26]. Blood is assumed to be an incompressible Carreau fluid, non-Newtonian, and the Navier-Stokes equation is used as the governing equation for the flow of blood. The equation system for time-dependent three-dimensional incompressible flow of a generalised Newtonian fluid can be represented as,

$$\frac{\partial u_i}{\partial t} + u_i \frac{\partial u_i}{\partial x_j} = \frac{1}{\rho}\frac{\partial}{\partial x_j}\sigma_{ij} \tag{1}$$

$$\frac{\partial u_i}{\partial x_i} = 0, i, j = 1, 2, 3 \tag{2}$$

where $u_i, i = 1, 2, 3$ are velocity components in the cartesian and $x_i, i = 1, 2, 3$ are the three components; σ_{ij} is the component of the stress tensor; ρ is the fluid density, which is constant $1060 kg/m^3$ for incompressible fluid. Eqs. (1) and (2) govern the momentum and continuity fluid for an incompressible, respectively. The following constitutive equation defines the component of the stress tensor as:

$$\sigma_{ij} = -p\delta_{ij} + \tau_{ij} \tag{3}$$

$$\tau_{ij} = \mu\left[\frac{\partial u_i}{\partial x_j} + \frac{\partial u_j}{\partial x_i}\right] \tag{4}$$

where p, and δ_{ij} are pressure and Kronecker delta ($\delta_{ij} = 1$ for $i = j$, otherwise $\delta_{ij} = 0$) and μ is the shear rate dependent dynamic viscosity, which is determined by different constitutive correlations depending on the type of fluid being considered. These correlations vary for Newtonian and non-Newtonian fluids, which is discussed in Section 2.2.2. Therefore, using Eqs. (3) and (4) the incompressibility, the Navier-Stokes Eq. (1) become,

$$\frac{\partial u_i}{\partial t} + u_i \frac{\partial u_i}{\partial x_j} = -\frac{1}{\rho}\frac{\partial p}{\partial x_j} + \frac{\mu}{\rho}(\nabla^2 u_i) + \frac{1}{\rho}\left(\frac{\partial \mu}{\partial x_j}\left(\frac{\partial u_i}{\partial x_j} + \frac{\partial u_j}{\partial x_i}\right)\right)$$

$$\frac{\partial u_i}{\partial x_i} = 0, i, j = 1, 2, 3 \tag{5}$$

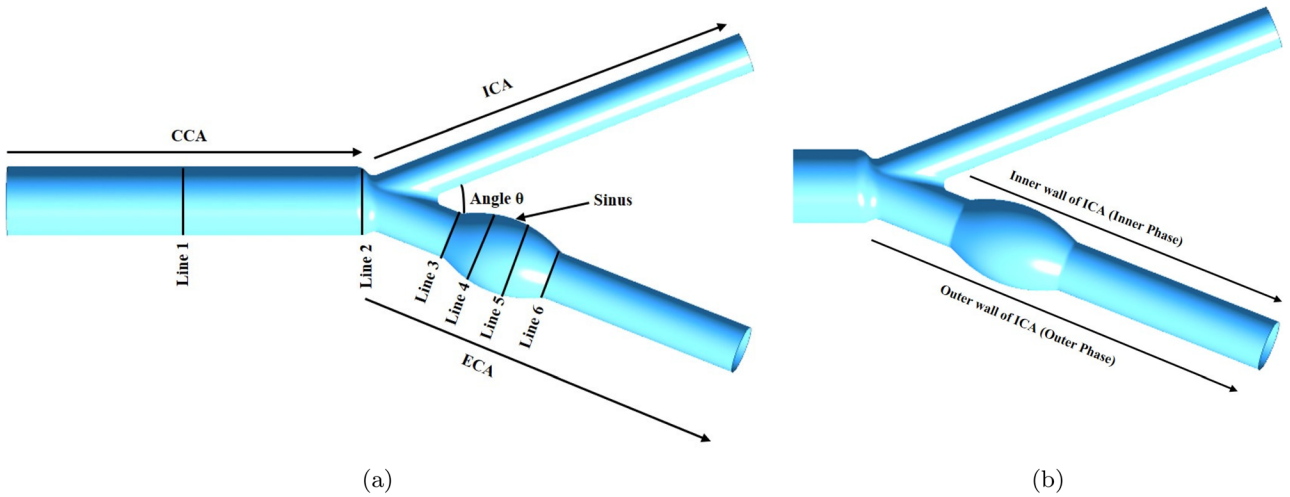

Fig. 2 Geometry of the human carotid artery bifurcation. **a** Line 1, Line 2, Line 3, Line 4, Line 5, and Line 6 show the flow cross-section level; **b** Inner and outer wall of the ICA

The velocity and pressure can be obtained from the equation system Eq. (5) by applying appropriate boundary and initial conditions.

2.2.2 Non-newtonian blood

The value of the dynamic viscosity is determined by specific constitutive correlations, which depend entirely on what kind of fluid it is. The experimental data for non-Newtonian blood exhibit that the viscosity of blood is dependent on the shear rate [27–29]. Numerous methodologies have been introduced to explain non-Newtonian impacts in blood flow estimations [30]. At a higher shear rate greater than $1s^{-1}$, the Eq. (6) fits the blood data perfectly to describe the dynamic viscosity. The shear rates to be expected are higher than $1s^{-1}$ based on available carotid bifurcation flow research. The viscosity is accounted for in blood by employing the Carreu model, represented as the following equation:

$$\mu = \mu_\infty + (\mu_0 - \mu_\infty)\left(1 + (\lambda\dot{\gamma})^2\right)^{(n-1)/2} \tag{6}$$

Here, λ is the relaxation time, μ_0 is dynamic viscosity at zero strain rate, and μ_∞ dynamic viscosity at infinity strain rate and n is the power index [28, 31, 32]. The parameters listed in Table 1 are used to simulate the viscosity model for non-Newtonian blood behavior.

Figure 3 clearly describes the shear-thinning behaviour of the blood in the Carreau model. According to this, at a lower shear rate, the viscosity is greater, whereas when the shear rate increases, the viscosity of blood tends to conform to the Newtonian model.

2.2.3 Boundary conditions

The generalised 3-dimensional Navier-Stokes system Eq. (5) can be computed by imposing appropriate boundary and initial conditions. For our research, we used realistic boundary conditions that mimic the pulsatile flow, which imitates the blood flow in the human body, and defined the UDF in Fluent. Therefore, at the inlet of the CCA, a transient flow rate profile is proposed. The flow profile is the combination of systole and diastole depicted in Fig. 3, where the systole is $0 < t < 0.218\ s$ indicates the rapidly increasing maximum inflow rate, and the diastole phase is $0.218 < t < 0.5\ s$. The sine wave has the peak velocity 0.5

Table 1 Coefficients for the Non-Newtonian model [33]

Non-Newtonian	Carreau model cofficient
	$\mu_0 = 0.056 Pa.s$
	$\mu_\infty = 0.0035 Pa.s$
	$\lambda = 3.313 s$
	$n = 0.3568$

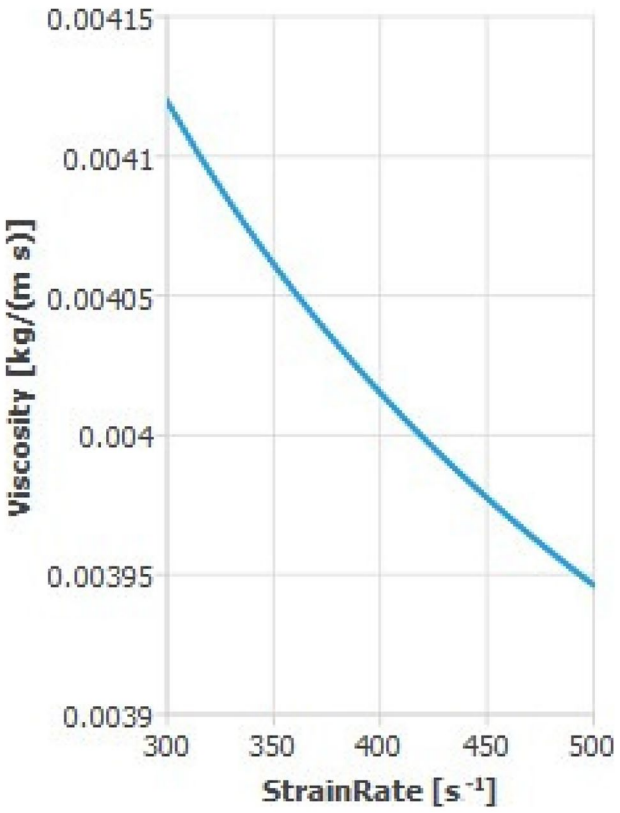

Fig. 3 Relation between Viscosity and shear rate for Carreau Non-Newtonian model

m/s in the systolic phase, and the minimum velocity is 0.1 m/s with the duration of 0.5 m/s. In order to describe inlet pulsatile blood flow more precisely, the UDF function in Fluent is given by the following equation: [34];

$$u(t) = \begin{cases} 0.5\sin[4\pi(t + 0.0160236)] : & 0.5n < t \le 0.5n + 0.218 \\ 0.1 : & 0.5n + 0.218 < t \le 0.5(n+1) \end{cases}, n \in \mathbf{N} \tag{7}$$

Ideally, a Windkessel type model should be implemented as the outlet boundary condition at the outlet [35, 36]. In this study, we do not consider physiological criteria for using the appropriate terminal resistance to control the flow of blood at the outlet. So, at the pressure outlet, we have imposed a simpler gauge pressure 0 or 13, 332 $Pa.s$ with natural outflow, while the wall is considered as rigid so that a no-slip boundary condition is imposed there.

2.2.4 Numerical method

A commercial ANSYS fluent finite volume programme is used to formulate the simulations governing equations. The QUICK approach is used for spatial discretization, and the SIMPLEC algorithm is adopted to model

the velocity-pressure interaction (Semi Implicit Method for Pressure-Linked Equations Consistent). This method is a modified method of the SIMPLE algorithm. This algorithm was originally proposed by Van Doormal and Raithby [37]. The variables are computed at the cell centre, with input provided by four neighbouring cells. The following equation represents the algebraic approximation of the integral balance for the P dependent on neighbouring cells for the discrete value of Φ,

$$a_P\Phi_P = a_E\Phi_E + a_W\Phi_W + a_N\Phi_N + a_S\Phi_S + F_\Phi \tag{8}$$

where, subscript P denotes the cell centre and superscript E, W, N and S, are the neighbouring grid points, and F_Φ is a source term. Other than convection and diffusion, a source term could include the pressure gradient, boundary conditions, or any other impact [17]. The processes for finding the solution are as follows:

1. The correct pressure and velocity are considered to be equal to the current pressure and velocity plus corrections,

$$u = u^* + u'; \tag{9}$$

where, u^* and u' are the guessed velocity field and the velocity correctively.

2. To derive a relationship between the velocity and pressure corrections, the correction relation and the momentum equations were used,

$$u = u^* + D(\Delta p'); \tag{10}$$

3. Discretization of the continuity equation for the control volume,

$$(\rho Au)_W - (\rho Au)_E + (\rho Av)_S - (\rho Av)_N = 0; \tag{11}$$

where A is the area of the cell face in the equation.

4. Substitution for the velocities u and v in Eq. (11), leads to

$$a_P p'_P = a_E p'_E + a_W p'_W + a_N p'_N + a_S p'_S + F; \tag{12}$$

where, $S = (\rho Au^*)_W - (\rho Au^*)_E + (\rho Av^*)_S - (\rho Av^*)_N = 0$ [37].

So, when momentum calculations are done in their corrected form, the velocity correction is obtained. A sufficiently fine time step of 0.01 was taken. For every variable, the solution convergence criteria were adjusted to 10^{-6}.

2.2.5 Turbulence model- the standard $k-\varepsilon$

The following transport equation yields the general form of the turbulence kinetic energy, $k-\varepsilon$. ε represent its rate of dissipation:

$$\frac{\partial}{\partial t}(\rho k) + \frac{\partial}{\partial x_j}(\rho k u_i) = \frac{\partial}{\partial x_i}\left[\left(\mu + \frac{\mu_t}{\sigma_k}\right)\frac{\partial k}{\partial x_j}\right] + G_k + G_b - \rho\varepsilon - Y_M + T_k \tag{13}$$

$$\frac{\partial}{\partial t}(\rho \varepsilon) + \frac{\partial}{\partial x_j}(\rho \varepsilon u_i) = \frac{\partial}{\partial x_i}\left[\left(\mu + \frac{\mu_t}{\sigma_\varepsilon}\right)\frac{\partial \varepsilon}{\partial x_j}\right] + B_{\varepsilon_1}\frac{\varepsilon}{k}(G_k + B_{\varepsilon_3}G_b) - B_{\varepsilon_2}\rho\frac{\varepsilon^2}{k} + T_\varepsilon \tag{14}$$

where, G_k in the above equation is the generation of turbulence kinetic energy by the velocity gradient. Due to buoyancy, the turbulence kinetic energy in the standard $k-\epsilon$ turbulence model is denoted by G_b. Y_m denotes the role of the variable dilation in compressible turbulence in the total dissipation rate. $B_{\varepsilon_1}, B_{\varepsilon_2}$ and B_{ε_3} are constants. The turbulent Prandlt numbers for k, ε are given by σ_k and σ_ε , respectively in Eqs. (13) and (14). T_k and T_ε are user-defined source terms. The turbulent viscosity, μ_t, is computed by combing k and ε as follows [33]:

$$\mu_t = \rho B_\mu \frac{k^2}{\varepsilon} \tag{15}$$

where, B_μ is a constant. The model constants Table. Table 2 were employed, in order to model the transport model.

2.2.6 Hemodynamic descriptors

WSS measurements are crucial for keeping monitoring of blood flow in arteries. Understanding cardiovascular diseases requires careful observation of the intensity and volatility of WSS, a crucial indicator of the force that blood exerts on artery walls. The WSS is computed at each point in the cardiac cycle and then averaged within the region of interest (ROI), either spatially or temporally, to obtain the Time-Averaged Wall Shear Stress (TAWSS). The resultant Time-Averaged Wall Shear Stress Magnitude (AWSS), in addition, provides important details on the general effect of blood flow on artery walls. These hemodynamic characteristics enable the creation of suitable treatments that prevent cardiovascular health by giving important insights into prospective cardiovascular risk factors.

Table 2 The values of model constants

Constants	Values
B_{ε_1}	1.44
B_{ε_2}	1.92
B_μ	0.09
σ_k	1.0
σ_ε	1.3

$$TAWWS = \frac{1}{T}\int_0^T |\overline{WSS}|dt \tag{16}$$

Where, WSS is the instantaneous vector of shear stress imparted by blood to the artery walls, and T is the period of one pulse cycle. Moreover, the Oscillatory Shear Index (OSI) is an important parameter that reflects the variations in Wall Shear Stress (WSS) over time and quantifies the difference between the Time-Averaged Wall Shear Stress (AWSS) and the Time-Averaged Wall Shear Stress Vector (AWSSV). OSI measures the degree of fluctuation in shear stress during a pulsating cycle. In simpler terms, it indicates how much the shear stress varies back and forth within each pulsation cycle. The formula used to compute OSI is as follows,

$$OSI = 0.5 \times \left(1 - \frac{|\int_0^T \overline{WSS}dt|}{\int_0^T |\overline{WSS}|dt}\right) \tag{17}$$

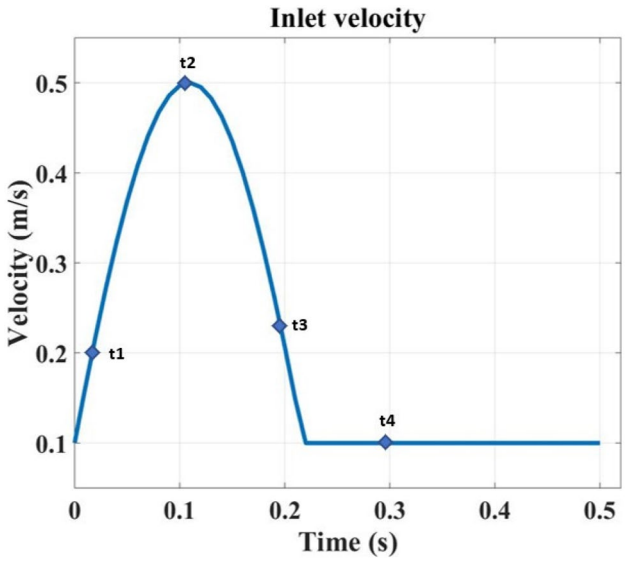

Fig. 4 Pulsatile inlet velocity cycle

3 Result and Discussion

The impact of bifurcation angle and sinus shape on flow behaviour is investigated using the computational results. The hemodynamic factors simulations for three different geometries differ in their bifurcation angle, and the sinus shapes are discussed in this section. These parameters affected the velocity profile, pressure , WSS, TAWSS and OSI. As previously mentioned, the same boundary conditions are applied for the simulation of each model. Since the boundary conditions are the same at both outlets, the resistance of the downstream vasculature affects how much flow is distributed across the outlets. Thus, the geometry of the bifurcation mostly determines how the flow separates. The velocity streamline distribution of these three models is shown in Fig. 5 at the four representative time steps. The figure of streamline velocity distribution implied that more recirculations occurred at the late systole ($t3$). At the peak systole ($t2$) and after the diastole ($t4$), there is no backflow was observed. The study selected specific axial positions to illustrate the flow of blood, namely the middle common carotid artery (CCA), the bifurcation, and four distinct axial positions within the sinus. These positions are visually depicted in Fig. 2 of the paper. At the same positions, the axial velocity was investigated for the other two models. Fig. 7 represents the axial velocity at these six axial positions along with the diameter of the referenced blood vessel. Due to the initial condition, the axial velocity is depicted as a periodic flow pattern. Fig. 7a-r presents the x-velocity component on these six lines at four distinct time steps during a cardiac cycle, as demonstrated in Fig. 4. In all models, the velocity profile at the middle of the CCA and at bifurcation is highest at time $t2$, which is peak systolic, and the velocity profile tends to be almost parabolic from model 1 to model 3 as shown in Fig. 7a-f. The velocity profile is slanted towards the inner phase of the carotid artery wall and became flattered at the outer wall when it moved from line 3 to line 6 as in Fig. 7.

Indeed, transient or unstable flow separation that causes flow disturbance zones at branches, bifurcations, and curves in the arterial circulation contributes to a propensity for atherosclerosis. In this study, the distribution of flow parameters in carotid artery models was examined by analyzing the axial velocity contour at specific points during the pulse cycle. Fig. 6 presents the contour plots of axial velocity on different axial slices of these carotid artery models at four distinct time steps, highlighting the presence of flow disturbances. Upon observation, it was found that the flow in model 1 artery remained undisturbed after the early systole, indicating a consistent and uniform flow pattern. This can be attributed to the absence of any unsteady flow conditions in this model. In model 2 artery, a certain level of flow disturbance was noted throughout the cardiac cycle, except during the early systole phase. Similarly, model 3 carotid artery exhibited a similar pattern of disturbed flow, but with a more pronounced interruption. It was observed that the extent of flow interruption increased with the bifurcation angle of the artery. Notably, negative axial velocity was observed in the slice at the bifurcation, indicating the presence of blood recirculation in that region. The recirculation zone can also be identified by examining the streamlines shown in Fig. 5. Furthermore, the velocity profiles exhibited minimal variation between the different models, as depicted in Fig. 6.

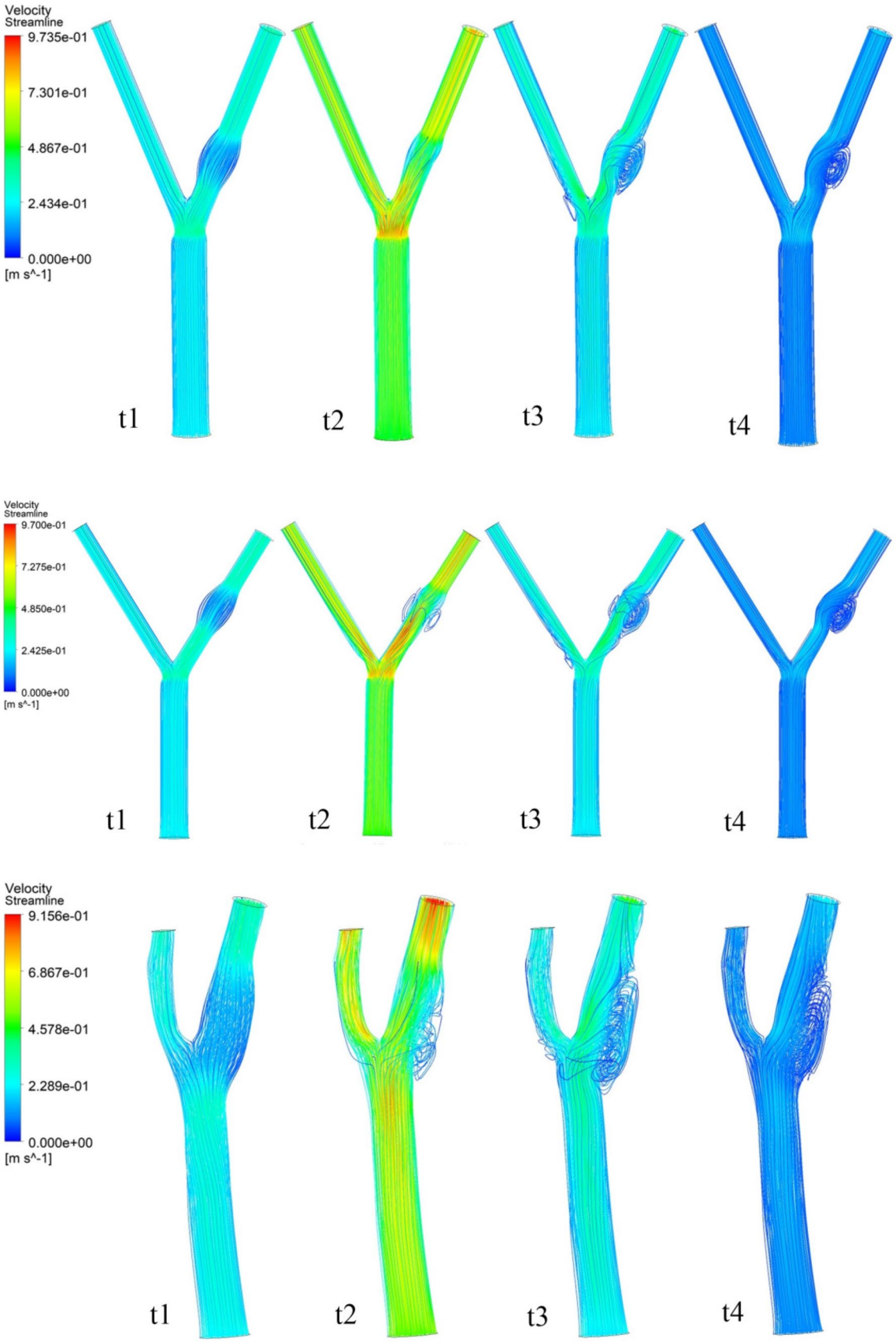

Fig. 5 Velocity streamlines distribution at four different times $t1$ = early systole, $t2$ = peak systole, $t3$ = late systole and $t4$ = mid diastole

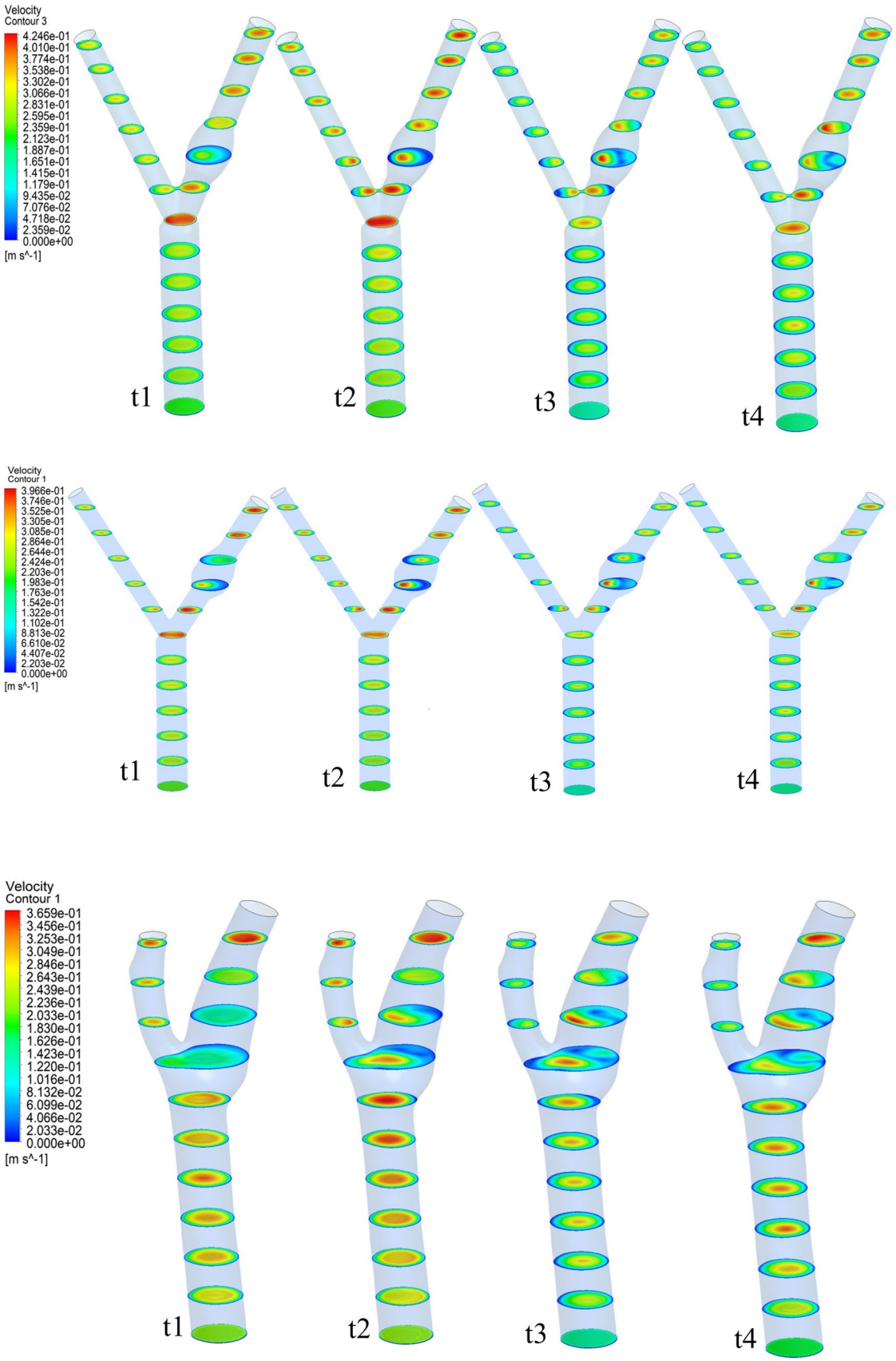

Fig. 6 Axial velocity profile on different axial slices at four different times $t1$ = early systole, $t2$ = peak systole, $t3$ = late systole and $t4$ = mid diastole

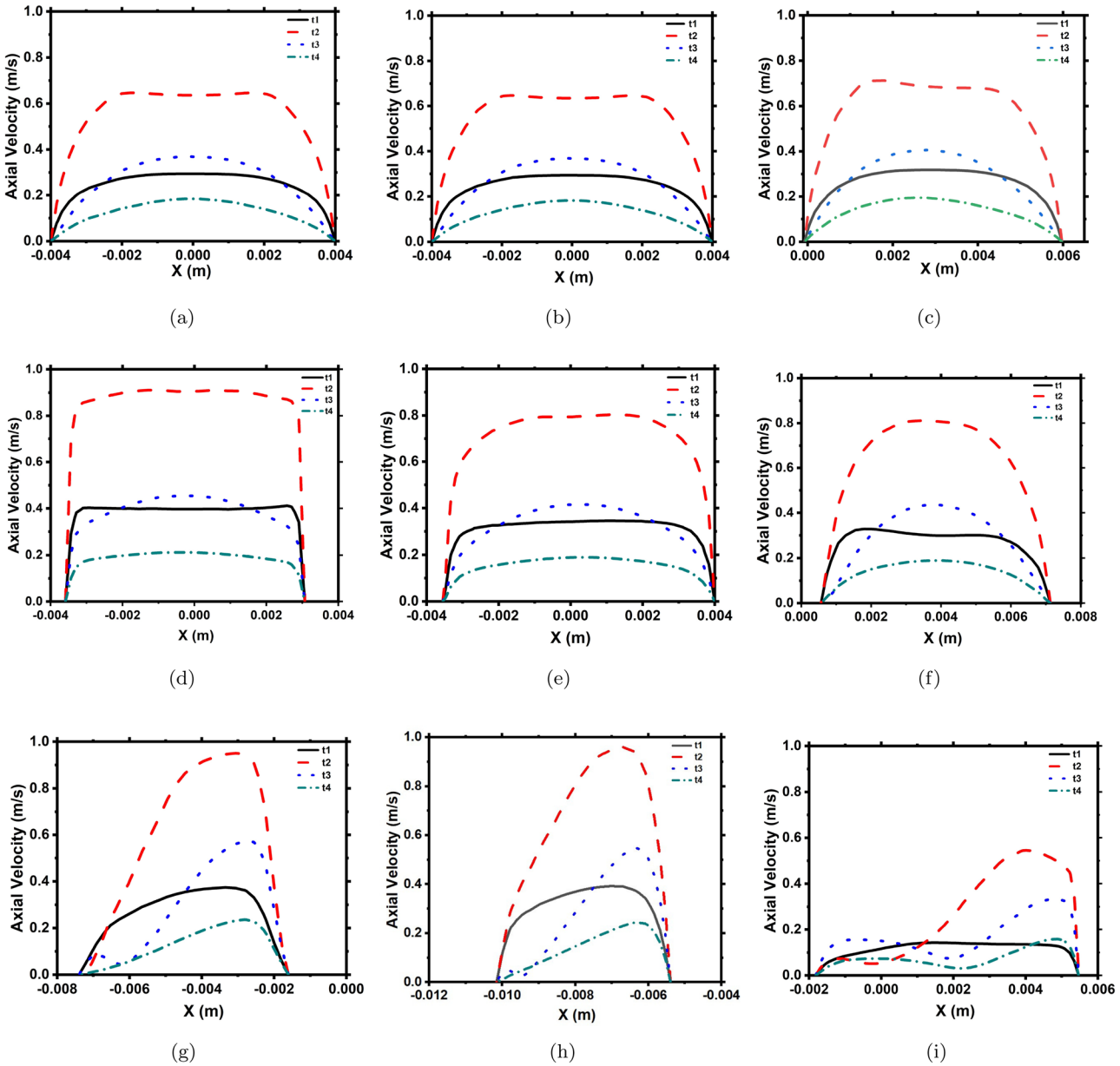

Fig. 7 Axial velocity profile for lines 1,2,3,4,5 and 6 of models 1,2 and 3

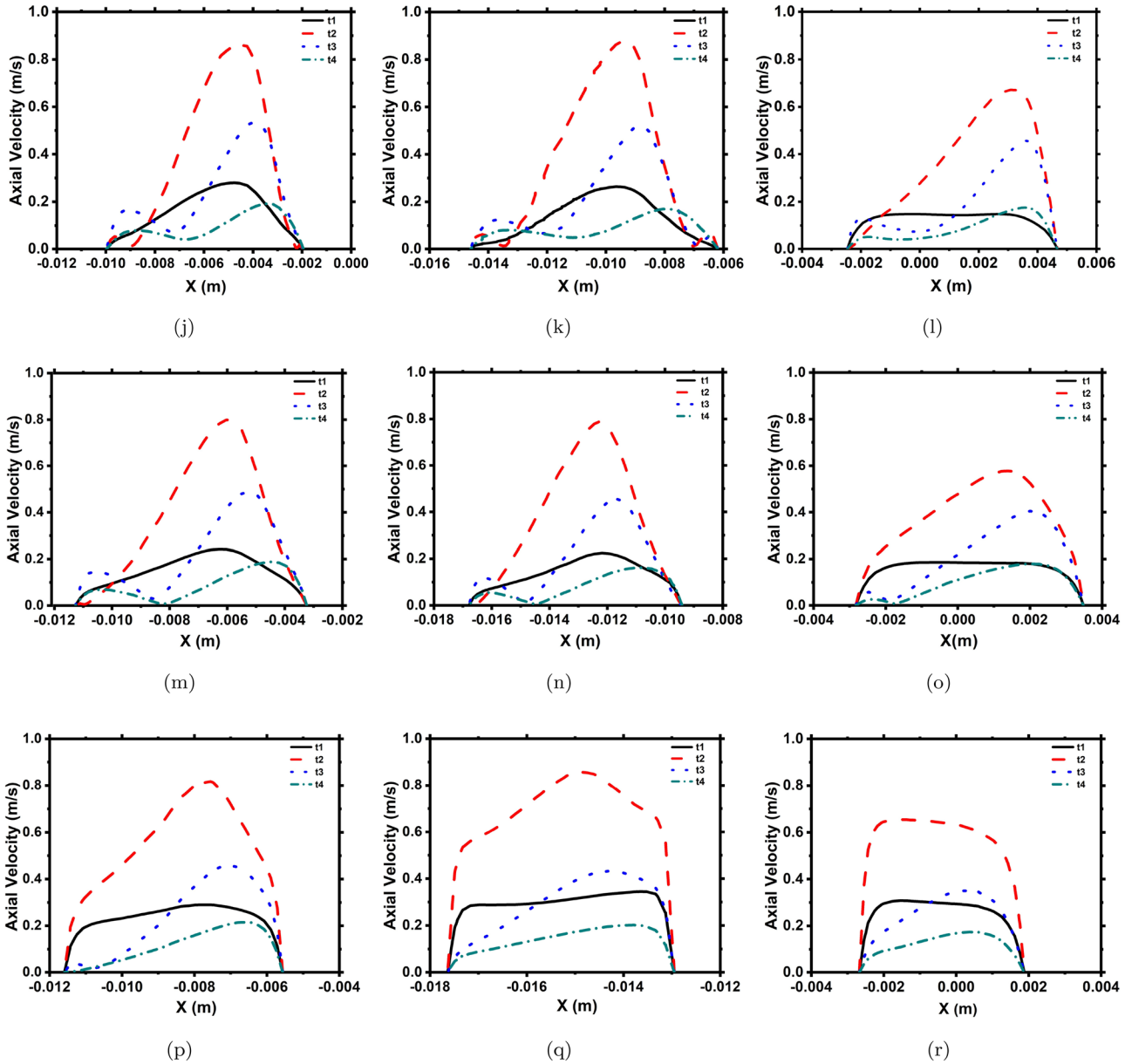

Fig. 7 (continued)

A stroke may occasionally be brought on by excessive blood pressure, which causes arteries to burst and exert pressure on the nearby brain tissues on account of haemorrhage. High blood pressure-related complications include the thickening of the arterial wall. Additionally, it is asserted that the detrimental effect of high blood pressure is greater than that of low shear stress and that the strain of the artery in reaction to high blood pressure might result in atheroma [38]. Thus, in Fig. 8, at the four distinct time steps that are early systole, peak systole, late systole, and diastole, the contour pressure distributions are illustrated for all the carotid artery models. All models have uniform and variable pressure that varies somewhat over the geometry. At the sinus and bifurcation, significant pressure variations are seen, yet all models produce the same conclusion. The bifurcation, where there is a sudden shift in velocity, is where the highest pressure occurs, corresponding to the maximum shear stress. On the wall of the sinus section of the ICA branch, blood pressure doesn't vary significantly and constantly stays at a moderate level. The specific site where the external carotid artery (ECA) transitions into the internal carotid artery (ICA) corresponds to a notable increase in blood pressure within the carotid artery apex. Additionally, compared to the walls of the ECA zone, the pressure on the ICA region's walls

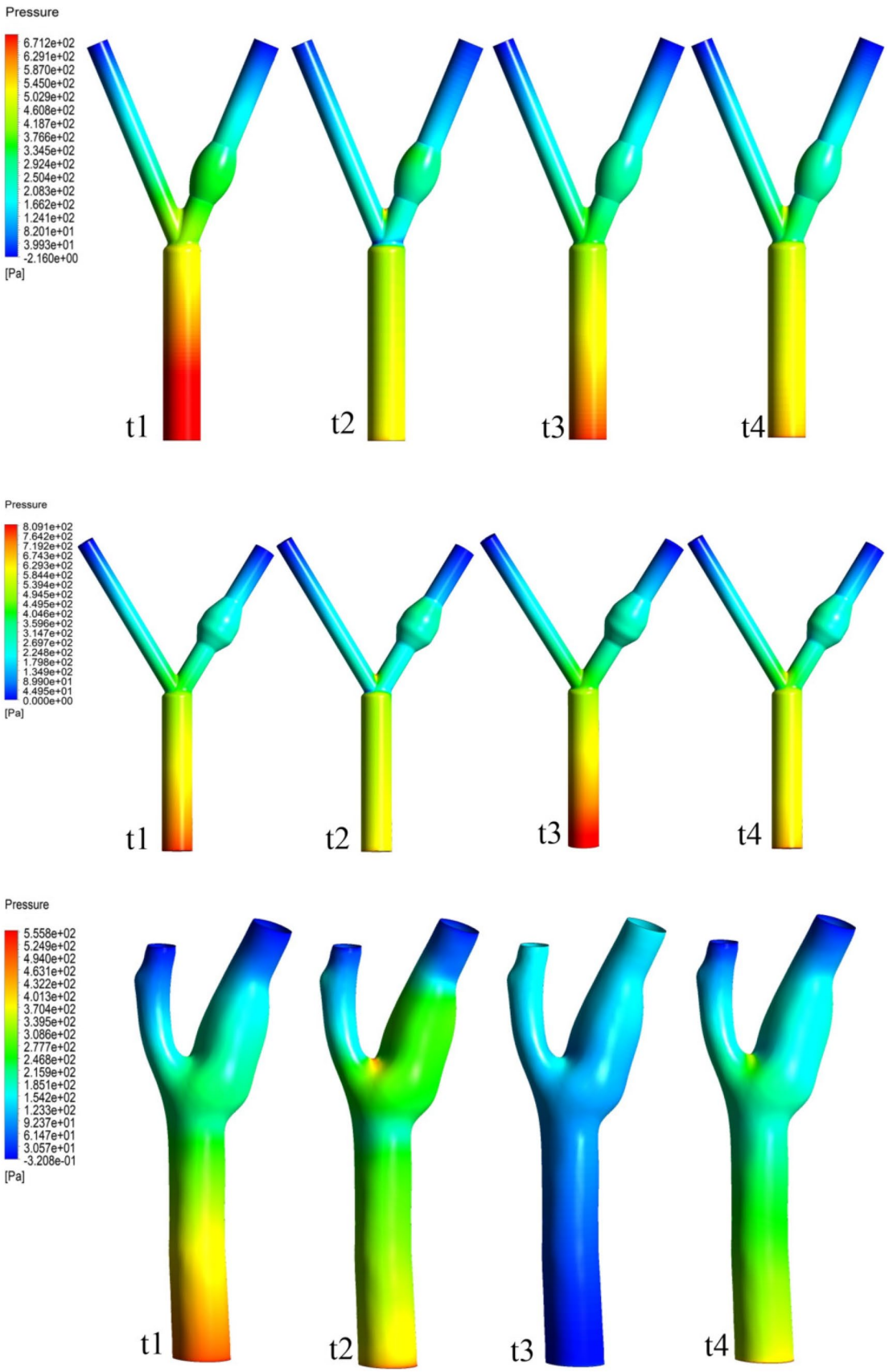

Fig. 8 Pressure contour for four different times $t1$ = early systole, $t2$ = peak systole, $t3$ = late systole and $t4$ = mid diastole

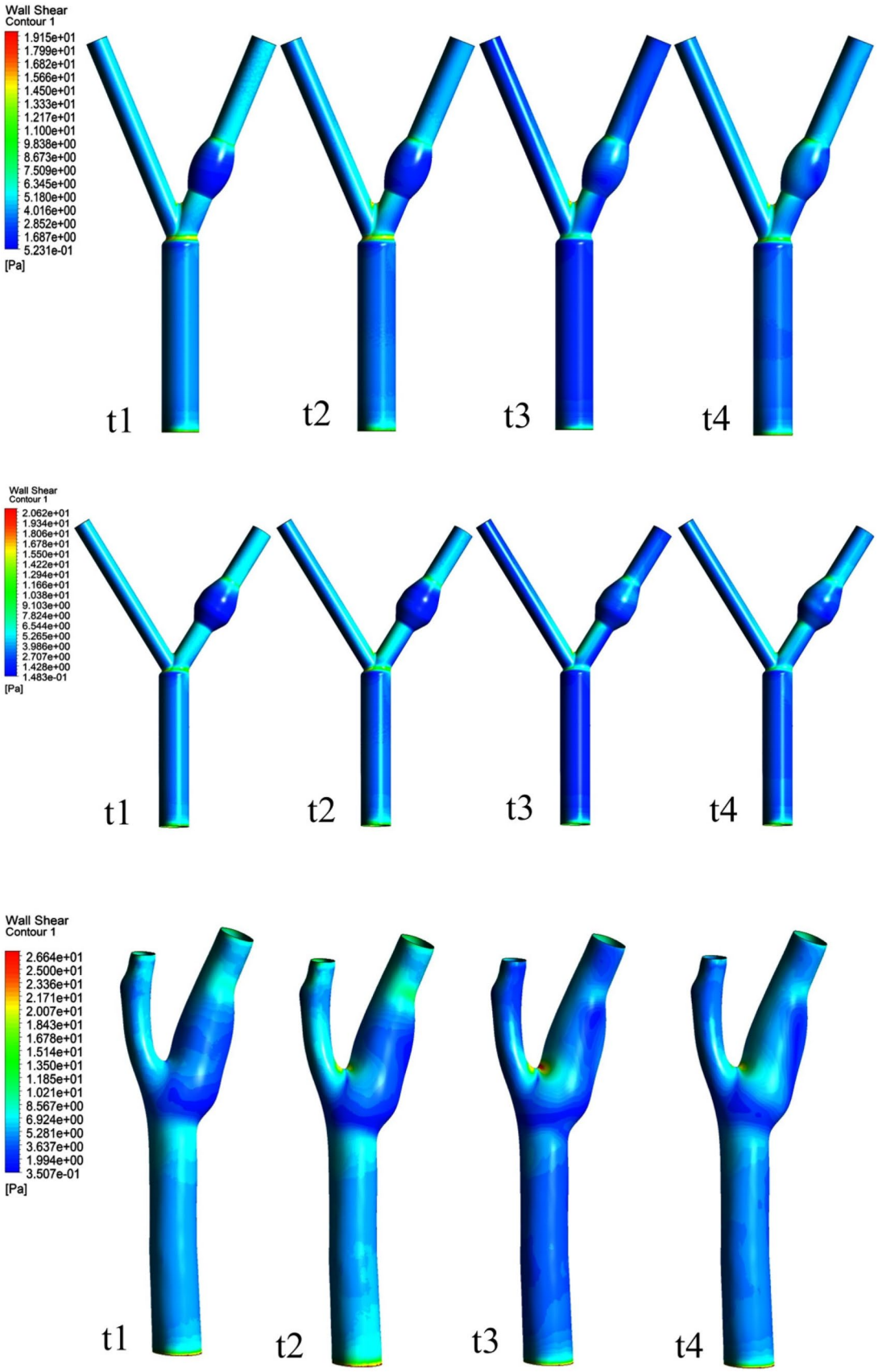

Fig. 9 WSS magnitude at four different times $t1$ = early systole, $t2$ = peak systole, $t3$ = late systole and $t4$ = mid diastole

is greater. Although the pressure difference was the same at the boundary between the inlet and outlet borders, the pressure drop and flow resistance generally increased as the bifurcation angle rose for the same flow rate. The pressure in the model 2 is higher than the model 1 at the apex of the carotid artery and at the proximal part of the ICA and ECA. Furthermore, because the model 3 has a smaller bifurcation angle than the models 1 and 2, it has less pressure drop. Consequently, with an increasing bifurcation angle, there was a corresponding decrease in the flow rate. This reduction in flow rate was particularly pronounced during the diastolic phase, characterized by lower flow rates, resulting in reduced variations in flow rate.

Figure 9 shows a comparison of WSS magnitude contours for different carotid artery models that are different in the bifurcation angle and sinus shape at four distinct time steps in one cardiac cycle. The distribution illustrates the intricate flow pattern that has been formed around the bifurcation. On the distal side of the bifurcation, where the flow separates, a strong WSS spatial gradient is particularly evident at peak and late systoles. Since model 3 has a smaller bifurcation angle than models 2 and 3, it is obvious that the WSS is substantially greater in this model. Hence, when the value at a specific time steps is compared for these models, the WSS value decreases as the bifurcation angle decreases for peak systole and late systole. However, there is no definite pattern found in shear stress. WSS plots for these three models on the inner and outer phases of the ICA at early, peak, and late systole are shown in Fig. 10a-h. Fig.2b represents the inner and outer phases of the ICA wall. At each time step, the WSS for all three models is high in the inner phase and low in the outer phase of the ICA wall. The absence of a negative WSS suggests that no reverse flow occurred at that region. Almost zero WSS occurs during the early systole at the sinus position for all the models. The peak value of WSS is found in the carotid artery just after the sinus position, where the diameter of the artery reduces. The velocity gradient of the blood increases close to the wall of the artery, which causes the sudden rise of WSS. The variation of the WSS is least at the sinus position of the carotid artery, where recirculation occurs more. The value of the peaks changes with the change in bifurcation angle along with the length.

Furthermore, there is no impact of bifurcation angle on WSS at the outer wall, despite the fact that the downstream variation of WSS on the outside wall is identical to that for the inner wall. WSS's magnitude, meanwhile, is less at the outer wall. According to the computational fluid dynamics data in the current study, the carotid artery, which has a smaller bifurcation angle, had low WSS values. The low WSS value represents the likelihood that atherosclerosis may develop. For smaller bifurcation angles in the carotid artery, the value of WSS is lowest.+

The study analyzed two WSS-derived parameters: TAWSS and OSI. These parameters were calculated for all timesteps in the simulations. Fig. 11 shows the contour plot of time-averaged wall shear stress for four different time steps and under various geometric conditions. The distribution of TAWSS values, revealing a high value at the significant narrowing observed at the ECA branch, at region before bifurcation and at immediately after the sinus. On the other hand, Fig. 11 showed low TAWSS values downstream of stenotic locations, particularly in the potential atherosclerosis-prone area. The significant influence of geometric factors, especially bifurcation angle and sinus shape, on TAWSS distribution in the carotid artery. The lower TAWSS values observed in Model 2, characterized by a larger bifurcation angle and cylindrical sinus shape, may indicate reduced mechanical forces on the arterial wall, potentially elevating the risk of atherosclerosis development. Conversely, the higher TAWSS in Model 3, attributed to a smaller bifurcation angle and a normal sinus shape. Meanwhile, during the cardiac cycle, the highest TAWSS values were observed at peak systole t_2 in each model, specifically, 1.453×10^3 in model 3, 1.307×10^3 in model 2, and 1.234×10^3 in model 1. On the other hand, the lowest TAWSS values occurred during late systole t_4, with values of 2.598×10^1 in model 3 ,8.245 for model 2 and 2.693×10^1 in model 1.

Figure 12 displays the contour plot of the OSI for four different time steps and under various geometric conditions. The results for OSI Fig. 12 demonstrated high values downstream of CCA stenosis and carotid bulb stenosis (ICA plaque area). When fluid flow is purely oscillatory, the OSI reaches its maximum value of 0.5. Model 2 attributes wider bifurcation angles and cylindrical sinus shapes to higher OSI values 4.960×10^{-1}. The model 1 attained 4.959×10^{-1} value. Meanwhile, model 3 attributes smaller bifurcation angles and normal sinus shapes to lower OSI values 4.954×10^{-1}. An OSI of 0.5 indicates that the flow is perfectly reversing, with equal magnitudes of flow in opposite directions during each oscillation cycle. As the shear stress acting in the opposite direction increases, the OSI value also increases. This suggests that the flow becomes more disturbed and less steady, with a higher degree of flow reversal during the oscillations. This often occurs in regions where flow separation and recirculation take place. In these regions, the OSI tends to reach its highest values. In essence, as the opposing shear stress in the flow intensifies, the OSI also rises, reaching its peak in regions of flow separation and recirculation, where the flow changes direction during each oscillation. The OSI at the branched artery is influenced by the angle at which the artery bifurcates because of the fluctuation of the WSS over time. The OSI value shows an direct relationship with the bifurcation angle, meaning that as the angle increases, the OSI tends to increase. The variations in the OSI are attributed to changes in the sinus shape, which occur due to differences in the geometric properties of the artery's branching structure.

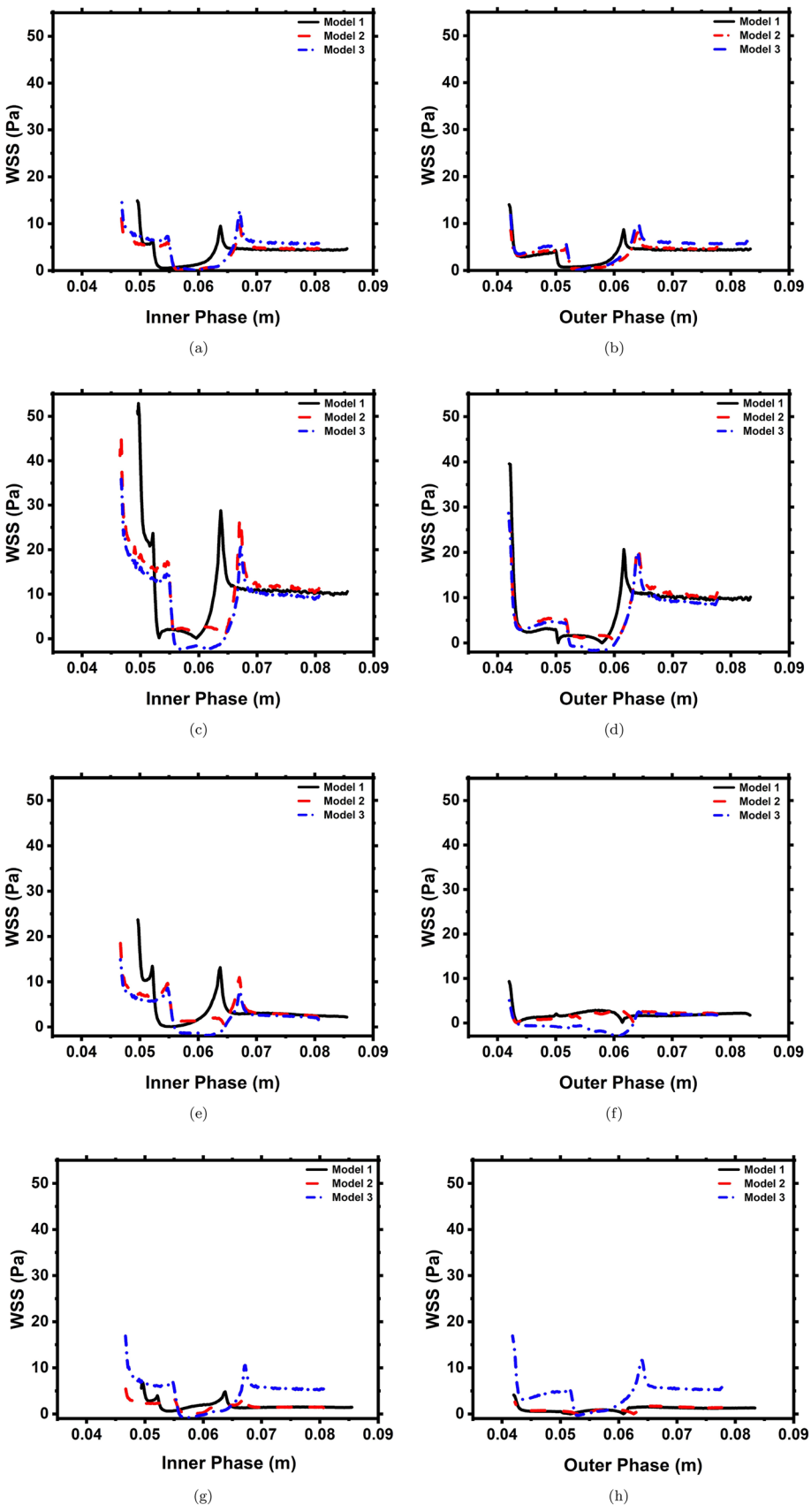

Fig. 10 WSS for the model 1,model 2 and model 3 during the cardiac cycle along the inner phase and the outer phase of ICA wall at diiterent time steps; **a** and **b** for early systole (t1); **c** and **d** for peak systole (t2); **e** and **f** for late systole (t3), and **g** and **h** for early systole (t4)

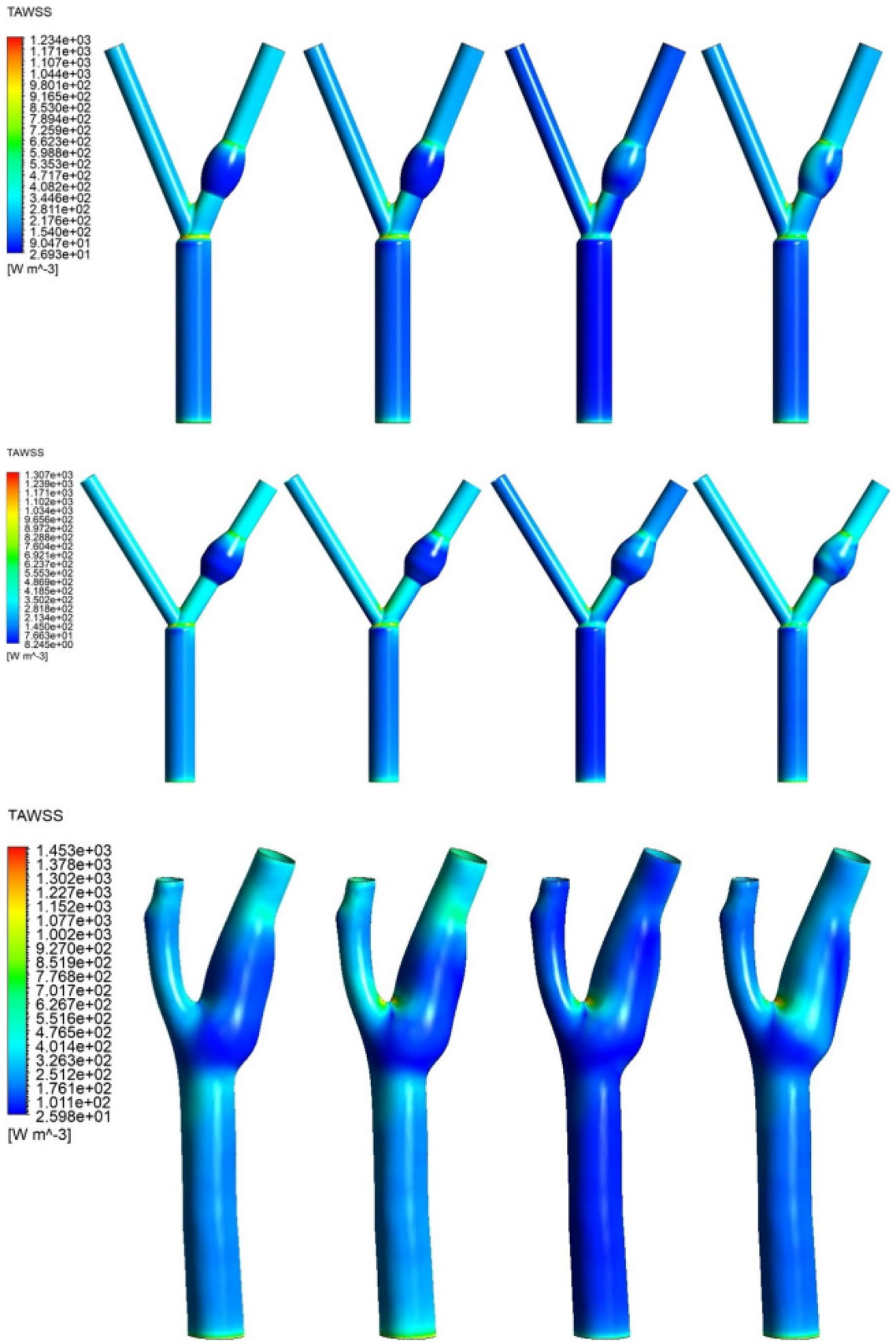

Fig. 11 TAWSS contour for four different times $t1$ = early systole, $t2$ = peak systole, $t3$ = late systole and $t4$ = mid diastole

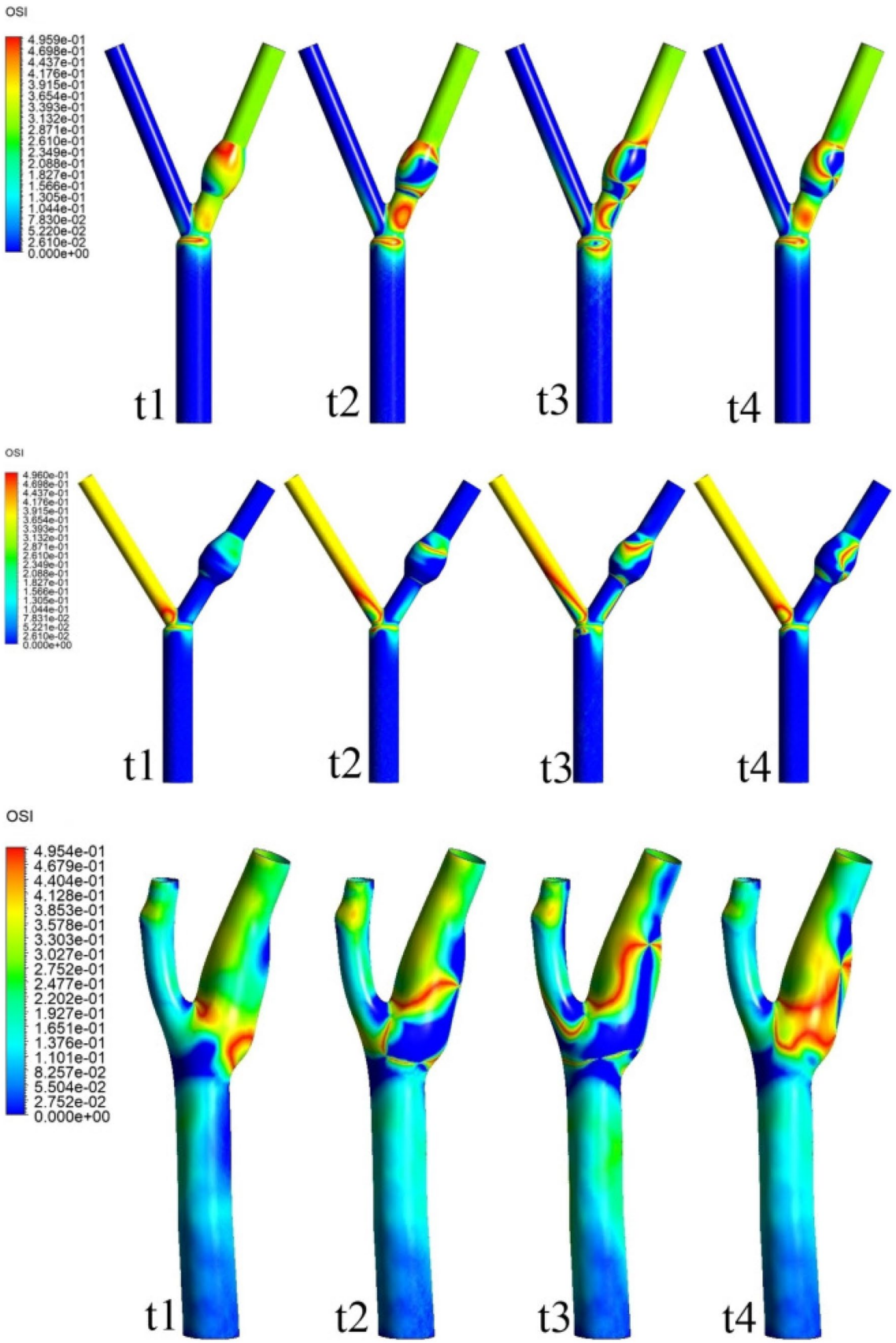

Fig. 12 OSI contour for four different times $t1$ = early systole, $t2$ = peak systole, $t3$ = late systole and $t4$ = mid diastole

4 Conclusion

The geometrical characteristics of blood vessels can significantly influence arterial hemodynamics, which refers to the study of the forces that regulate blood flow through arteries. In the present study, investigation were performed on the combined effects of variable bifurcation angles and sinus shapes on atherosclerosis formation in bifurcation geometries. According to current findings, the distinctive shape of the carotid artery is believed to play a significant role in promoting mechanical factors that contribute to the onset of diseases. The impact of this unique geometry is primarily due to the alterations it causes in the blood flow pattern within the artery. Due to flow separation at the carotid bifurcation, which shows the same pattern as the stenosed curved channel, the WSS at the outer wall is significantly less than that at the inner wall during the whole cardiac cycle. Due to poor WSS, the outside wall is more susceptible to atherosclerosis than the inner wall. In this article, blood flow in three distinct human right carotid arteries is transiently studied using a non-Newtonian blood viscosity model. When these three arteries are compared, it becomes clear that the distribution of wall shear stress creates intricate patterns on the arterial wall that fluctuate significantly over the cardiac cycle. However, it appears that throughout a significant amount of the cardiac cycle, low wall shear stress is foremost at the proximal end of the artery for all arteries. Further down the artery, there is a higher wall shear stress, specifically at the arterial bends and narrowing. Low-wall shear stress is produced by sudden expansions during the majority of the cardiac cycle. This study also highlights the critical role of geometric factors in determining TAWSS distribution and OSI in the carotid artery.

The findings indicated that the probability of atherosclerotic plaque development is increased in areas like the posterior wall of the inner carotid artery sinus where shear stress occurs at a low rate, velocity is decreasing, and substantial particle sedimentation exists. The possibility that atherosclerosis will develop is indicated by the low WSS score. The value of WSS is lowest in carotid arteries with wider bifurcation angles. High TAWSS values are observed at specific locations in the carotid artery, including the significant narrowing observed at the ECA branch, at the region before bifurcation and immediately after the sinus, likely referring to the widened area carotid artery. The lower TAWSS values observed in Model 2, characterized by a larger bifurcation angle and cylindrical sinus shape, while the higher TAWSS in Model 3, attributed to a smaller bifurcation angle and a normal sinus shape. Moreover, the results shows the maximum TAWSS values occurring at peak systole and the minimum TAWSS values occurring at late systole for each model. When the bifurcation angle is wider, and the shape of the sinus (the curvature of the artery) is more cylindrical, the OSI value tends to be higher. This implies a more disturbed and reversing flow pattern, while in this case, when the bifurcation angle is smaller, and the sinus shape is closer to a normal or typical shape, the OSI value tends to be lower. This indicates a more regular and less disturbed flow pattern. From these result, we concluded that when the bifurcation angle decreased, several flow variables experienced an increase in their values due to small pressure drops in the flow field. The change in the bifurcation angle and sinus shaped had an impact on the WSS at the inner wall of the artery, TAWSS at the ECA branch, at region before bifurcation and at immediately after the sinus and the OSI at the branched artery. However, interestingly, the bifurcation angle had no effect in the region of stenosis. The high TAWSS values suggest the presence of strong mechanical forces acting on the arterial wall due to the blood flow patterns. Such high forces could have distinct physiological effects on the artery. These results are provided with the presumption that the flow is being studied using a fixed mesh. There may be some disagreement if the simulations were performed on a model with elasticity in the arterial walls and the artery was allowed to move with the heart rate.

Acknowledgements This research work is supported by the Science and Engineering Research Board (SERB; Grant ECR/2017/000831) and the Department of Science and Technology (DST), Government of India, for the grant to accomplish this research. All authors are grateful to SERB-DST for funding support.

Declarations

Conflicts of interest The authors declare that there is no competing financial of interest.

Human and Animal Rights The authors declare that there are no competing financial interests. This article does not contain any studies with human or animal subjects performed by the authors.

References

1. Avolio A, Butlin M, Walsh A (2010) Arterial blood pressure measurement and pulse wave analysis-their role in enhancing cardiovascular assessment. Physiol Meas 31:R1-47
2. Perktold K, Thurner E, Kenner T (1994) Flow and stress characteristics in rigid walled and compliant carotid artery bifurcation models. Medical & Biological Engineering & Computing (MBEC) 32:19–26
3. Singh D, Singh S (2022) A multi-scale computational study of pulsatile flow in the three- dimensional human carotid artery bifurcation. Series on Biomechanics 36:38–54
4. Singh D, Singh S (2023) Mathematical modelling of an incompressible, Newtonian blood flow for the carotid artery. pp 259–272
5. Ku D, Giddens D, Zarins C, Glagov S (1985) Pulsatile flow and atherosclerosis in the human carotid bifurcation. arteriosclerosis. Arteriosclerosis 5:293–302

6. Marshall I, Zhao S, Papathanasopoulou P, Hoskins PR, Xu YX (2004) MRI and CFD studies of pulsatile flow in healthy and stenosed carotid bifurcation models. J Biomech 37(5):679–87
7. Morris PD, Narracott A, Tengg-Kobligk HV, Soto DAS, Hsiao S, Lungu A, Evans P, Bressloff NW, Lawford PV, Hose DR, Gunn JP (2016) Computational fluid dynamics modelling in cardiovascular medicine. Heart 102
8. Arjmandi-Tash O, Razavi S, Zanbouri R (2011) Possibility of atherosclerosis in an arterial bifurcation model. Bioimpacts 1:225–8
9. Lee B (2011) Computational fluid dynamics in cardiovascular disease. Korean Circ J 41:423–30
10. Rabbi M, Laboni F, Arafat MT (2020) Computational analysis of the coronary artery hemodynamics with different anatomical variations. 19
11. Perktold K, Peter R, Resch M, Langs G (1991) Pulsatile non-newtonian blood flow in three-dimensional carotid bifurcation models: A numerical study of flow phenomena under different bifurcation angles. J Biomed Eng 13:507–15
12. Dzavik V, Kharbanda R, Ivanov J, Ing D, Bui S, Mackie K, Ramsamujh R, Barolet A, Schwartz L, Seidelin P (2006) Predictors of long-term outcome after crush stenting of coronary bifurcation lesions: Importance of the bifurcation angle. Am Heart J 152:762–9
13. Sun Z, Cao Y (2011) Multislice CT angiography assessment of left coronary artery: Correlation between bifurcation angle and dimensions and development of coronary artery disease. Eur J Radiol 79:e90-5
14. Watanabe M, Uemura S, Dote Y, Sugawara Y, Goryo Y, Ueda T, Kawata H, Saito Y (2014) Bifurcation angle influences atherosclerotic plaque distribution in coronary arteries: An optical coherence tomography study. J Am Coll Cardiol 63:A1918
15. Ziyrek M, Sertdemir A, Duran M (2020) Effect of coronary artery bifurcation angle on atherosclerotic lesion localization distance to the bifurcation site. J Saudi Heart Assoc 32:399–407
16. Tada S (2019) Computational study of the influence of bifurcation angle on haemodynamics and oxygen transport in the carotid bifurcation. Biomed Eng: Appl, Basis Commun 31:1950024
17. Ro K, Ryou H (2009) Numerical study of the effects of periodic body acceleration (pgz) and bifurcation angle in the stenosed artery bifurcation. Korea-Australia Rheol J 21:175–183
18. Momin M, Ara N, Arafat MT (2020) Analysis of blood flow patterns to estimate atherosclerosis formation in the left carotid artery by CFD simulation
19. Zalud NC, Bulusu KV, Plesniak MW (2023) Shear stress metrics associated with pro-atherogenic high-risk anatomical features in a carotid artery bifurcation model. Clin Biomech 105
20. Rossmann J, Berger S, Saloner D (2002) Numerical analysis of flow through a severely stenotic carotid artery bifurcation. J Biomech Eng 124:9–20
21. Toloui M, Firoozabadi B, Saidi M (2012) A numerical study of the effects of blood rheology and vessel deformability on the hemodynamics of carotid bifurcation. Scientia Iranica 19:119–126
22. Perktold K, Peter R, Resch M, Langs G (1991) Pulsatile non-Newtonian blood flow in three-dimensional carotid bifurcation models: a numerical study of flow phenomena under different bifurcation angles. J Biomed Eng 13(6):507–515
23. Stratarys (2017) Grabcad. https://grabcad.com/
24. Nagargoje M, Gupta R (2020) Effect of sinus size and position on hemodynamics during pulsatile flow in a carotid artery bifurcation. Comput Methods Programs Biomed 192
25. Nguyen K, Clark C, Chancellor T, Papavassiliou D (2008) Carotid geometry effects on blood flow and on risk for vascular disease. J Biomech 41:11–9
26. Urquiza S, Blanco P, Vénere M, Feijóo R (2006) Multidimensional modeling for the carotid blood flow. Comput Methods Appl Mech Eng 195:4002–4017
27. Brooks D, Goodwin J, Seaman G (1970) Interactions among erythrocytes under shear. J Appl Physiol 28:172–7
28. Cho Y, Kensey K (1991) Effects of the non-Newtonian viscosity of blood on flows in a diseased arterial vessel. part 1: Steady flows. Biorheology 28:241–62
29. Razavi A, Shirani E, Sadeghi M (2011) Numerical simulation of blood pulsatile flow in a stenosed carotid artery using different rheological models. J Biomech 44:2021–30
30. Tu C, Deville M (1996) Pulsatile flow of non-Newtonian fluids through arterial stenoses. J Biomech 29:899–908
31. Caballero A, Laín S (2015) Numerical simulation of non-Newtonian blood flow dynamics in human thoracic aorta. Comput Methods Biomech Biomed Eng 18(11):1200–1216 (PMID: 24559110)
32. Johnston BM, Johnston PR, Corney S, Kilpatrick D (2004) Non-Newtonian blood flow in human right coronary arteries: steady state simulations. J Biomech 37(5):709–720
33. Moradicheghamahi J, Sadeghiseraji J, Jahangiri M (2018) Numerical solution of the pulsatile, non-Newtonian and turbulent blood flow in a patient specific elastic carotid artery. Int J Mech Sci 150
34. Sinnott M, Cleary P, Prakash M (2006) An investigation of pulsatile blood flow in a bifurcation artery using a grid-free method
35. Gharahi H, Zambrano B, Zhu DC, DeMarco JK, Baek S (2016) Computational fluid dynamic simulation of human carotid artery bifurcation based on anatomy and volumetric blood flow rate measured with magnetic resonance imaging. Int J Adv Eng Sci Appl Math 8:46–60
36. Wu Q, Xiaojie L, Lingjiao P, Weige T, Chunqi Q (2017) Simulation analysis of blood flow in arteries of the human arm. Biomed Eng: Appl, Basis Commun 29:1750031
37. Doormaal JPV, Raithby GD (1984) Enhancements of the SIMPLE method for predicting incompressible fluid flows. Numer Heat Transf 7:147–163
38. Augst A, Ariff B, Thom S, Xu X, Hughes A (2007) Analysis of complex flow and the relationship between blood pressure, wall shear stress, and intima-media thickness in the human carotid artery. Am J Physiol Heart Circ 293:H1031-7